



SIMULATION OF FOUR-POINT BENDING TESTS FOR THE VISCOELASTIC FRACTURE PROPERTIES OF CONCRETE

Tran Nam Hung *, Nguyen Thi Thu Nga

Le Quy Don Technical University, No. 236 Hoang Quoc Viet Street, Hanoi, Vietnam.

ARTICLE INFO

TYPE: Research Article

Received: 03/07/2023

Revised: 31/08/2023

Accepted: 10/01/2024

Published online: 15/01/2024

<https://doi.org/10.47869/tcsj.75.1.6>

* *Corresponding author*

Email: tranhung@lqdtu.edu.vn

Abstract. Understanding the fracture properties of concrete, such as crack propagation behavior and fracture energy, is crucial for designing and evaluating concrete structures. Experimental results are insufficient and cannot be directly employed for a comprehensive analysis of the fracture behavior of concrete structures under load, particularly when considering concrete as viscoelastic with the presence of cracks. Recognizing the time and cost constraints of traditional experimental testing, this research leverages numerical simulations as a cost-effective alternative to determine viscoelastic material parameters. Thus, the critical evaluation of concrete fracture properties, fundamental for the design and assessment of concrete structures, is addressed. Employing a finite element method for four-point bending tests, the study systematically investigates parameters such as initial crack depth, displacement acceleration, and time step. The material properties of concrete are described using viscoelastic models. The findings provide valuable insights into crack propagation behavior and deformation characteristics, emphasizing the significant influence of the modulus of elasticity on both maximum load values and displacement. These findings contribute to a deeper understanding of the structure's response and underscore the importance of considering these parameters in similar simulations. The study highlights the importance of considering these parameters in simulations to enhance the understanding of concrete fracture behavior. The paper's contributions can extend to optimizing concrete mixtures, formulating repair strategies, and improving structural assessments. Further research is suggested to improve the accuracy of simulations and investigate material properties under various conditions.

Keywords: Numerical concrete simulation, viscoelastic fracture properties, four-point bending test, initial crack-depth ratio.

1. INTRODUCTION

Concrete is one of the most widely used construction materials due to its excellent mechanical properties and durability. Understanding the fracture properties of concrete, such as crack propagation behavior and fracture energy, is crucial for designing and evaluating concrete structures. Fracture properties play a critical role in determining the structural integrity, serviceability, and safety of concrete structures under various loading conditions.

The evaluation of fracture properties of concrete has traditionally been conducted through experimental testing, which can be time-consuming, labor-intensive, and costly [1]. However, with the advancements in computational methods, numerical simulations have emerged as a valuable tool for predicting the fracture behavior of concrete. Numerical simulations offer the advantage of cost-effectiveness, flexibility in controlling test parameters, and providing insights into the underlying fracture mechanisms at different length scales [2].

In recent years, there has been a growing demand for research on fracture properties of concrete and the role of evaluating fracture parameters in concrete design and structural assessment, especially when concrete has the presence of Fiber-Reinforced-Plastic (FRP) reinforcement [3], or steel corrosion [4]. Accurate prediction of fracture properties can aid in optimizing concrete mixtures, developing effective repair and strengthening strategies for existing structures, and enhancing the durability and sustainability of concrete infrastructure. Therefore, the development and application of numerical simulation methods for studying fracture properties of concrete have gained significant attention in the field of civil engineering.

Nonlinear fracture mechanics has been developed, and various nonlinear fracture models have been proposed. However, these studies have primarily focused on three-point bending [5, 6]. In recent years, four-point bending (FPB) tests have been conducted on notched prismatic specimens to investigate the fracture behavior of new concrete, such as concrete/epoxy interfaces [7], or fiber-reinforced concrete [8] for experimental tests or steel-fiber-reinforced concrete in simulation [2].

For studying concrete behavior, both the three-point bending test and the four-point bending test are available options. The three-point bending test creates a stress concentration mainly at the loading point's center, whereas the four-point bending test generates a more uniformly distributed stress distribution. This latter approach provides advantageous circumstances for examining non-homogeneous materials like concrete, [9]. Choosing the four-point bending test for simulations improves precision and captures intricate deformation patterns more accurately compared to the three-point bending test. Therefore, opting for the four-point bending test is chosen in this study.

In this context, this paper aims to present a simulation approach for evaluating the fracture properties of concrete using four-point bending tests. The paper will discuss the significance of studying fracture properties of viscoelastic concrete and the important role of evaluating fracture parameters in concrete design and structural assessment. The proposed simulation approach and its potential applications in predicting the fracture behavior of concrete structures will be highlighted, along with a discussion on the challenges and future directions in this research area.

2. EXPERIMENTAL PROGRAM

2.1. Materials and numerical model

In the field of concrete creep behavior, viscoelastic models are commonly employed to describe the material's response, accounting for both elastic and viscous properties. Prominent models utilized in concrete creep analysis include the Burger model, Kelvin-Voigt model, and Maxwell model. These models are utilized to capture the time-dependent deformation of concrete under sustained loads, considering factors such as load magnitude, time duration, temperature, and moisture content.

The numerical simulation method used in this study involves finite element method, with the concrete modelled as a Burgers viscoelastic material. The input parameters for the concrete model include the compressive strength $f_c = 40.78$ MPa and elastic modulus $E = 32.46$ GPa, Poisson's Ratio $\nu = 0.2$.

For the creep behavior of concrete, which is modeled by using a rheological Burgers model, a class of 3D isotropic NALV (Non-Aging Linear Viscoelastic) is assumed in this study. The Burgers model consists of multiple elements connected in series, including Maxwell and Kelvin series, to capture both elastic and viscous responses of the material, with 6 parameters as following: k_M^e, μ_M^e bulk and shear moduli of the Maxwell series of the concrete; k_K^e, μ_K^e bulk and shear moduli of the Kelvin series of the concrete; $\eta_{M(K)}^s, \eta_{M(K)}^d$: bulk and shear viscosities parties of the concrete.

In this model, the concrete is assumed to be isotropic and independent of direction (3D), meaning that the elastic properties do not vary with the direction of the material. This model is widely used to describe the elastic behavior of materials such as concrete, polymers, rubbers, and other elastic materials. In this study, it can be used to simulate and predict the viscoelastic behavior of concrete under time-dependent deformation conditions. The elastic and viscous stiffness are defined by the following fourth-order tensors:

$$C_M^e = 3k_M^e J + 2\mu_M^e K, C_M^v = \eta_M^s J + \eta_M^d K, C_K^e = 3k_K^e J + 2\mu_K^e K, C_K^v = \eta_K^s J + \eta_K^d K \quad (1)$$

$$\text{Noted that } \frac{1}{E_M} = \frac{1}{9k_M^e} + \frac{1}{3\mu_M^e}; \frac{1}{E_K} = \frac{1}{9k_K^e} + \frac{1}{3\mu_K^e}.$$

The elastic and viscous compliance tensors S_M^e, S_M^v are related to the Maxwell part by: $S_M^e = \frac{1}{3k_M^e} J + \frac{1}{2\mu_M^e} K, S_M^v = \frac{1}{\eta_M^s} J + \frac{1}{\eta_M^d} K$.

The behavioral law of this model reads:

$$(C_K^e \cdot S_M^v) \sigma + (I + C_K^e \cdot S_M^e + C_K^v \cdot S_M^v) \dot{\sigma} + C_K^v \cdot S_M^e \ddot{\sigma} = C_K^e \dot{\varepsilon} + C_K^v \ddot{\varepsilon} \quad (2)$$

In the symbolic space of Laplace-Carson, (2) is linear and given by:

$$(C_K^e \cdot S_M^v) \sigma^* + p(I + C_K^e \cdot S_M^e + C_K^v \cdot S_M^v) \sigma^* + p^2 C_K^v \cdot S_M^e \ddot{\sigma} = p C_K^e \dot{\varepsilon}^* + p^2 C_K^v \ddot{\varepsilon}^* \quad (3)$$

where 'p' represents a complex variable in the symbolic space.

Since the apparent “stress-strain” relation (3) can be written as $\sigma^* = C^* \varepsilon^*$ with $C^* = 3k_s^* J + 2\mu_s^* K$, so the apparent bulk and shear moduli for the safe material can be written as follows [10]:

$$k_s^* = \frac{1}{k_M^e} + \frac{1}{p\eta_M^s/3} + \frac{1}{k_K^e + p\eta_M^s/3}, \quad \mu_s^* = \frac{1}{\mu_M^e} + \frac{1}{p\eta_M^d/2} + \frac{1}{\mu_K^e + p\eta_K^d/2} \quad (4)$$

If the derived function of time \dot{a} is $\dot{a} \cong \frac{a(t+dt) - a(t)}{dt}$ and $\ddot{a} \cong \frac{a(t+dt) - 2a(t) + a(t-dt)}{dt^2}$,

the behavior of concrete (2) is written:

$$\begin{aligned} & (c_1 J + c_2 K) \sigma(t+dt) - (c_3 J + c_4 K) \sigma(t) + (c_5 J + c_6 K) \sigma(t) + (c_7 J + c_8 K) \sigma(t-dt) \\ & = (c_9 J + c_{10} K) (\varepsilon(t+dt) - \varepsilon(t)) - (c_9 J + c_{10} K) (\varepsilon(t) - \varepsilon(t-dt)) \end{aligned} \quad (5)$$

where

$$\begin{aligned} c_1 &= \frac{3k_K^e}{\eta_M^s} + \frac{1}{dt} \left(1 + \frac{k_K^e}{k_M^e} + \frac{\eta_K^s}{\eta_M^s} \right) + \frac{1}{dt^2} \frac{\eta_K^s}{3k_M^e}, \quad c_2 = \frac{2\mu_K^e}{\eta_M^d} + \frac{1}{dt} \left(1 + \frac{\mu_K^e}{\mu_M^e} + \frac{\eta_K^d}{\eta_M^d} \right) + \frac{1}{dt^2} \frac{\eta_K^d}{2\mu_M^e}, \\ c_3 &= \frac{1}{dt} \left(1 + \frac{k_K^e}{k_M^e} + \frac{\eta_K^s}{\eta_M^s} \right) + \frac{2}{dt^2} \frac{\eta_K^s}{3k_M^e}, \quad c_4 = \frac{1}{dt} \left(1 + \frac{\mu_K^e}{\mu_M^e} + \frac{\eta_K^d}{\eta_M^d} \right) + \frac{2}{dt^2} \frac{\eta_K^d}{2\mu_M^e}, \\ c_5 &= \frac{1}{dt^2} \frac{\eta_K^s}{3k_M^e}, \quad c_6 = \frac{1}{dt^2} \frac{\eta_K^d}{2\mu_M^e}, \quad c_7 = \frac{1}{dt} 3k_K^e + \frac{1}{dt^2} \eta_K^s, \quad c_8 = \frac{1}{dt} 2\mu_K^e + \frac{1}{dt^2} \eta_K^d, \\ c_9 &= \frac{1}{dt^2} \eta_K^s, \quad c_{10} = \frac{1}{dt^2} \eta_K^d. \end{aligned} \quad (6)$$

Due to the limited availability of parameters in experiments test, only two parameters, E and ν are known, the initial assumptions for the parameters of the 3D isotropic non-aging linear viscoelastic (NALV) model are specified as presented in Table 1. The values shown in the table have been adjusted iteratively after analyzing factors that affect the P-u curve. The goal of this iterative adjustment is to make the calculated elastic modulus (E), Poisson's ratio (ν), maximum load (P_{max}), and displacement (u) align more closely with the experimental data mentioned in reference [1].

Table 1. Material properties for numerical simulation.

E_M (Pa)	ν_M	η_M^s (Pa.s)	η_M^d (Pa.s)	E_K (Pa)	ν_K	η_K^s (Pa.s)	η_K^d (Pa.s)
32.46×10^9	0.2	22.0×10^{17}	7.75×10^{17}	37.7×10^9	0.2	15.2×10^{16}	2.54×10^{16}

The numerical simulation process for flexural testing of concrete specimens followed the dimensions of length \times width \times height ($L \times B \times H$) = 1000 mm \times 120 mm \times 200 mm with a span/depth ratio (S/H) of 4 ($S = 800$ mm). Five different initial crack-depth ratios of 0.2, 0.3, 0.4, 0.5, and 0.6 were considered.

The experimental model was subjected to displacement-controlled loading, with a constant midspan displacement of 0.05 mm/min or 8.33×10^{-7} m/s. The dimensions and loading configuration of the test specimen are illustrated in Figure 1, where D is the distance between the loading point and the support point, and $D=H=200$ mm.

- Midspan deflection was evaluated as the load changed.
- Crack opening displacement was also considered during the loading process.

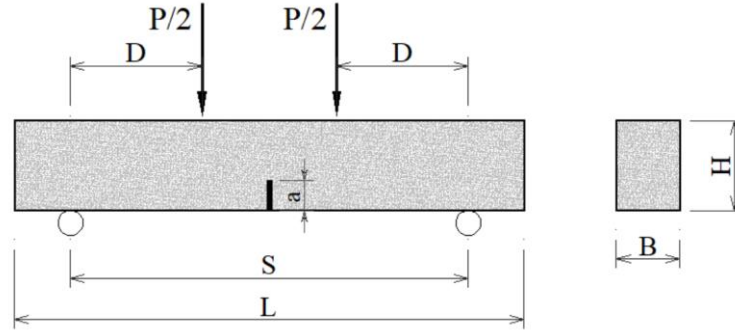


Figure 1. Dimension and constraints of the beam.

2.2. Basic finite element method

Fracture energy G_f is a critical mechanical property used to quantify the resistance of a material to crack propagation under tensile loads. It is typically determined from the load-displacement curve of a growing crack during experimental testing. Fracture energy serves as an indicator of a material's toughness or brittleness, reflecting the amount of energy required to extend a crack. It can be calculated or measured based on geometric properties of the crack, such as crack length or cross-sectional area. The characterization of fracture energy is essential for evaluating the mechanical behavior and durability of materials in various practical applications, including construction, hard materials, and composite materials. The fracture energy value, as reported in reference [1], is 201.285 N/m.

Levin et al. [15] presented a theorem that can address the homogenization of linear elastic materials with pre-stress or initial deformation. Follow this theorem, macroscopic stress field at the time $(t + dt)$ is written in the form:

$$\sigma(t + dt) = C_{Bu}^{INC} \varepsilon(t + dt) + \sigma_{Bu}^p(t) \quad (7)$$

with $\sigma_{Bu}^p(t)$ the pre-stress, which concern the stress and strain at time t and given by:

$$\begin{aligned} \sigma_{Bu}^p(t) = & \left(\frac{c_3}{c_1} \mathbf{J} + \frac{c_4}{c_2} \mathbf{K} \right) \sigma(t) - \left(\frac{c_5}{c_1} \mathbf{J} + \frac{c_6}{c_2} \mathbf{K} \right) \sigma(t - dt) \\ & - \left(\frac{c_9}{c_1} \mathbf{J} + \frac{c_{10}}{c_2} \mathbf{K} \right) (\varepsilon(t) - \varepsilon(t - dt)) - C_{Bu}^{INC} \varepsilon(t) \end{aligned} \quad (8)$$

and the stiffness tensor of viscoelastic concrete: $C_{Bu}^{INC} = \frac{c_7}{c_1} \mathbf{J} + \frac{c_8}{c_2} \mathbf{K}$.

The research employed the open-source computation software Cast3M for simulating cracked concrete beams in 2D. Due to the symmetry of the considered problem, only a half of the model is considered as shown in Fig. 2. In this numerical simulation, the structural model employs linear triangular elements. The mesh has been sufficiently refined to ensure that the results do not deviate by more than 5% when the mesh is refined by a factor of 1/10 compared to the original mesh, allowing for efficient analysis without excessive time consumption. The mesh has been strategically densified, particularly in the region between the beam and underneath the concentrated load. In this example, the size of the region is equal to $H/100$. This arrangement enhances the accuracy of simulation while maintaining computational efficiency.

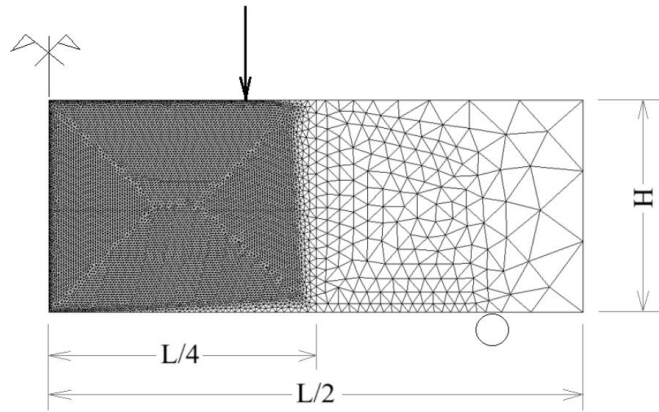


Figure 2. Meshing on CASTEM beams subjected to 4 point bending.

For the incremental algorithm, we effectuate as follows:

At $t = 0s$, instant response is elastic, $\sigma_1 = C_{Bu1}^{INC} \varepsilon_1$ with $C_{Bu1}^{INC} = C_K^e$.

At $t = dt$, the relation between σ_2 and ε_2 reads: $\sigma_2 = C_{Bu2}^{INC} \varepsilon_2 + \sigma_{Bu1}^p$.

where the pre-stress σ_{Bu1}^p given by (8) is concern of the stress and train σ_1 and ε_1 .

Once we have understood the behavior at $t = (i-1).dt$, we will find the behavior at time $t = i.dt$. Besides, the procedure for the fracture energy is as follows:

F is the motor force, and it is a function of P , L , H , B , and $g(a/H)$, $F = \frac{1}{E} \frac{9\pi l P^2 L^2}{4H^4 B^2} g(a/H)^2$ where P is the applied load on the beam, and $g(a/H)$ is a function of the crack length-to-beam height ratio (a/H), B is the thickness of the beam.

$$F = -\frac{\partial W}{\partial a} \quad (9)$$

where $W = \frac{1}{2} K(a) (\varepsilon - \varepsilon^v)^2 + W_{res}(a)$ and $K(a)$ represents the instantaneous elastic stiffness of the structure, $W_{res}(a)$ is an energy restitution. For more detail, the readers can see in [10].

Given the initial displacement of the applied load P as dU and the initial crack length as a_0 , the equation (9) is used to calculate the value of the motor force. F is then compared with the value of G_f . If $F < G_f$, the applied load displacement is increased by one proposed step of load. If not, it indicates that the crack has propagated, and the value of U needs to be recalculated for the increased value of F . This procedure is conditional on F exceeding the maximum allowable difference from G_f , denoted as e_0 (where e_0 is very small, on the order of 10^{-5} mm). Alternatively, if $F = G_f$, then the crack length a is increased by a predefined value. The crack length a is increased until it reaches the maximum value, a_{max} . If a has not reached a_{max} , the load continues increase. Besides, if the condition $F = G_f$ cannot be achieved, the increment of the load displacement step needs to be increased.

3. RESULTS AND DISCUSSION

The initially pre-existing crack with a length equal to 'a,' with values of 0.2H, 0.3H, 0.4H, 0.5H, and 0.6H, will propagate in a direction from the center of the beam straight upwards to the upper surface of the beam, creating a crack line. As the load increases, the crack causes the crack to grow almost to the entire height of the beam ($a_{max} = 0.98H$). Figure 3 shows that the displacement at mid-span is the highest. The flexural failure of the beam is mainly in the middle of the span, which is consistent with other experimental results.

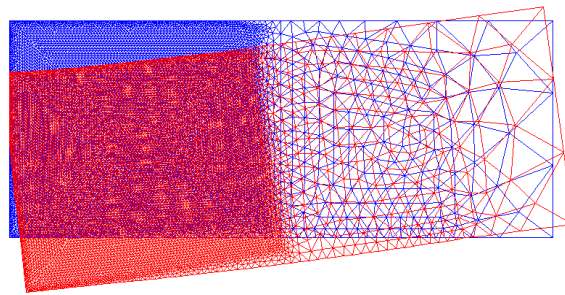


Figure 3. Deformation of a half of beam subjected to four-point bending.

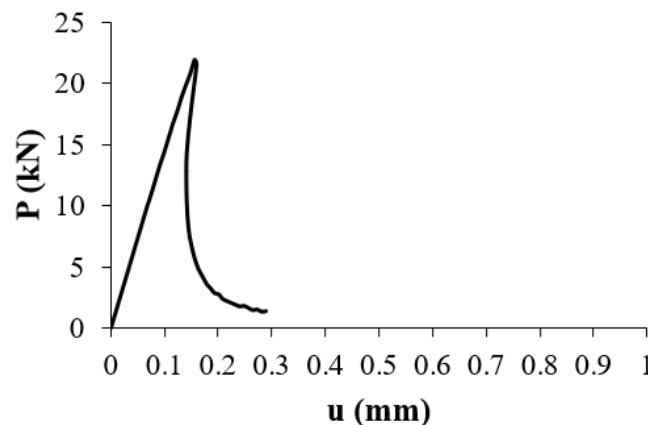


Figure 4. Numerical test result when the displacement is 0.05 mm/min.

The P-u curve in Figure 4 of the simulation model yields a maximum force value of 21.910 kN, which closely approximates the experimental value of $P_{max} = 21.956$ kN, as observed in [1]. Two distinct stages can be observed: the first stage exhibits nearly linear behavior reaching P_{max} with small displacements, while the second stage resembles a sloping

curve. After reaching P_{max} , the load value abruptly decreases significantly while the displacement does not increase significantly. This demonstrates the effective simulation capability of the software using the finite element method when it comes to capturing the limit load value P_{max} .

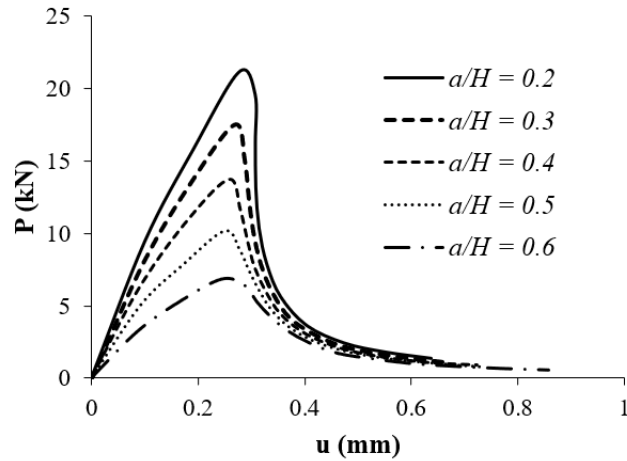


Figure 5. Load–displacement curves of concrete for five cases when the displacement is 0.6 mm/min.

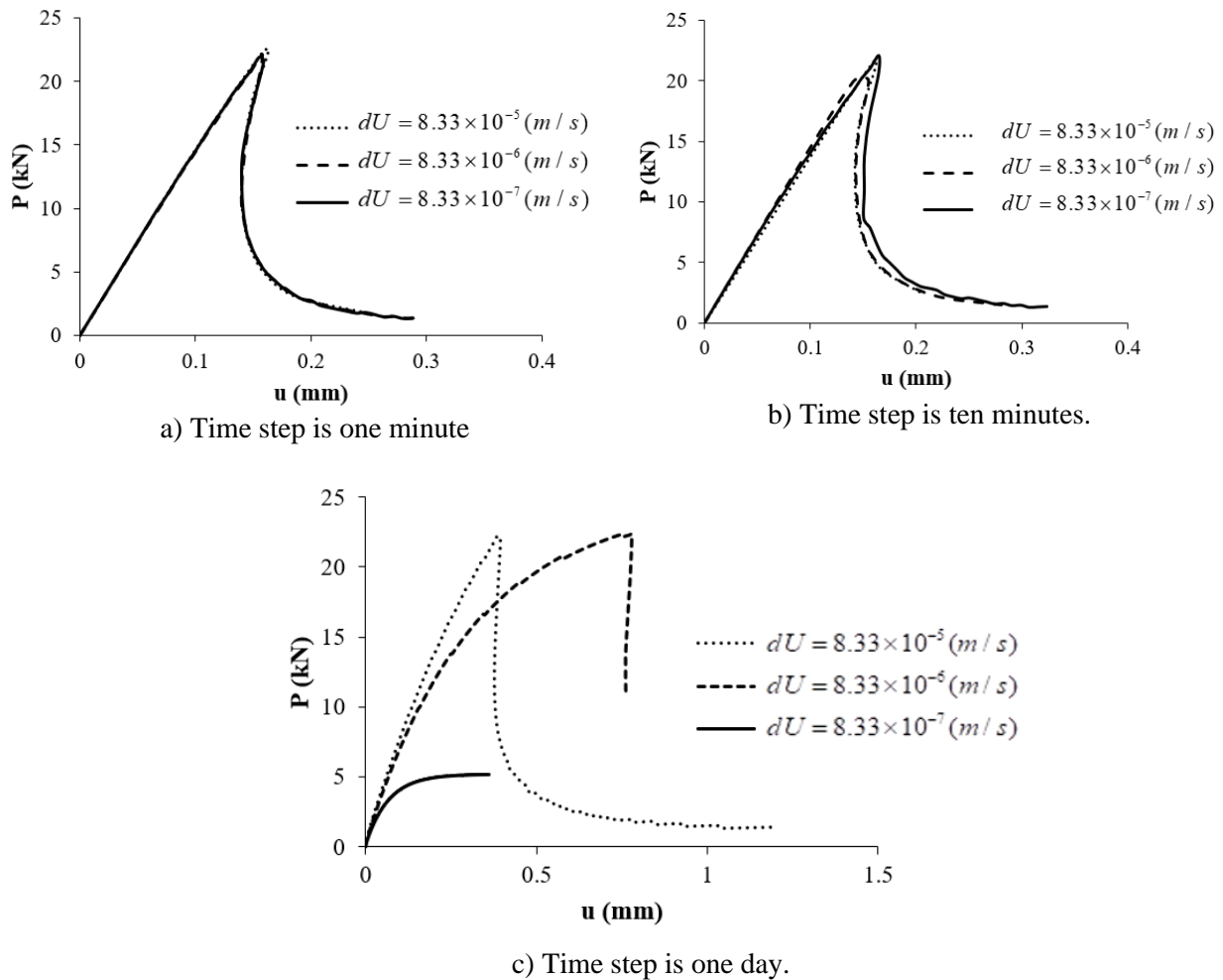


Figure 6. Force-displacement curves when the displacement acceleration value dU (m/s) changes.

Next, parameters such as the initial crack depth a , displacement acceleration dU , time step dt , fracture energy G_f , and 3D parameters will be investigated sequentially.

As shown in Figure 5, for cases where the initial crack-depth ratios were 0.4, 0.5 and 0.6, the P-u curve exhibited a softening behavior, indicating overall stability for the specimens. Notice that as the initial crack a increases, P_{max} decreases. However, for cases with initial crack-depth ratios of 0.2 and 0.3, a sudden drop in load occurred after a small descending segment following the peak load, indicating unstable crack propagation. Besides, it is evident that there is a significant increase in P when the initial crack value a is small. Additionally, the corresponding displacement value for P_{max} also shows a slight increase with the rising P , which is consistent with the experimental results.

To investigate the effect of displacement acceleration (dU), three cases of dU are studied when $a=0.2H$. Figure 6 demonstrates that P_{max} remains constant while the corresponding displacement value for P_{max} increases with decreasing values of the displacement acceleration dU . When the displacement acceleration is small, the structure exhibits larger displacements at the point of failure, as evidenced by the softer post-peak response in the graph after P reaches the same P_{max} .

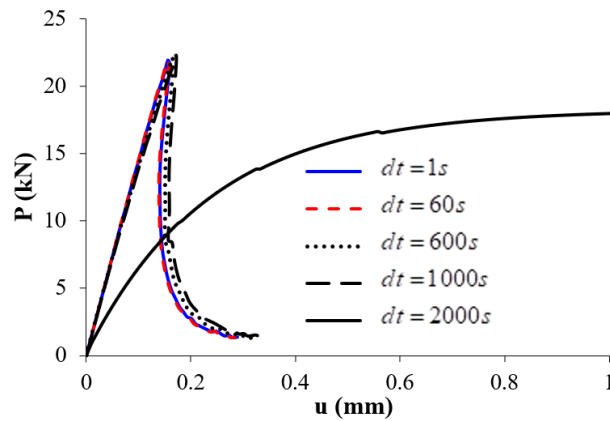


Figure 7. Force-displacement curves when the time step changes ($dU=8.33 \times 10^{-7} \text{m/s}$).

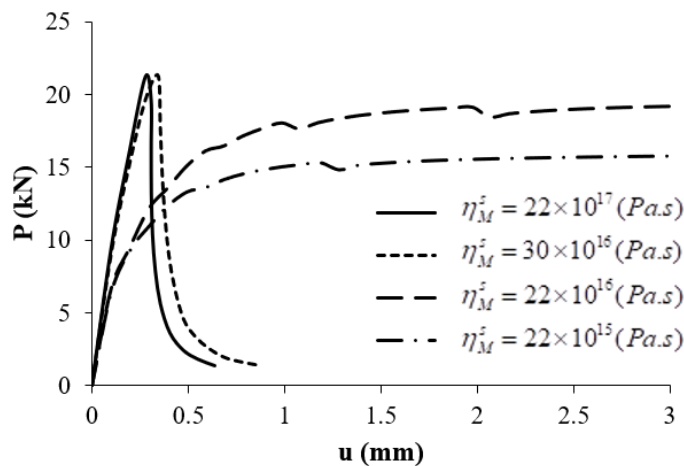


Figure 8. Force-displacement curves when the bulk viscosity of the Maxwell series changes.

Figure 6 illustrates that when the time step is one minute (Fig. 6a) or ten minutes (Fig. 6b), the variation of dU does not significantly alter the P-u curve. The beam behaves consistently as a case of crack propagation with a prominent P_{max} point that increases insignificantly, while dU increases by a factor of 100 from 8.33×10^{-7} m/s to 8.33×10^{-5} m/s. However, as can be seen in Figure 6c, when the time step is one day (or 86400s), dU significantly affects the behavior of the beam. Specifically, crack development occurs with a displacement in the bottom middle of the beam of 0.377 mm when dU is large (8.33×10^{-5} m/s), with the displacement of 0.74 mm when dU is decreased by a factor of 10, and no crack development when dU equals 8.33×10^{-7} m/s.

For the time step, observing Figure 7 reveals that when $dt=1s$ and $dt=60s$, the two P-u curves overlap each other. There is not much difference when increasing dt , specifically for $dt=600s$ and $dt=1000s$, the value of P_{max} remains unchanged. Only the slope of the initial stage of the P-u curve decreases slightly, and the curve becomes less steep after reaching P_{max} . However, when the time step is large ($dt=2000s$, approximately 0.55 hours), crack propagation does not occur, and the load value P reaches an asymptotic value of 18.17 kN, which is lower than P_{max} (21.91 kN).

The investigation of the influence of coefficient η_M^s reveals that when the coefficient decreases below its initial value, it affects the crack propagation results, as evident in Figure 8 where no crack development is observed in cases $\eta_M^s=22 \times 10^{15}$ (Pa.s) and $\eta_M^s=22 \times 10^{16}$ (Pa.s). Conversely, when the coefficient increases beyond $\eta_M^s=22 \times 10^{17}$ (Pa.s) the results remain unchanged, indicated by overlapping P-u curves.

The investigation of the influence of coefficient η_K^s reveals that it has minimal impact on the results, as evidenced by the nearly overlapping P-u curves in the pre- P_{max} stage and negligible differences after reaching P_{max} (Fig. 9).

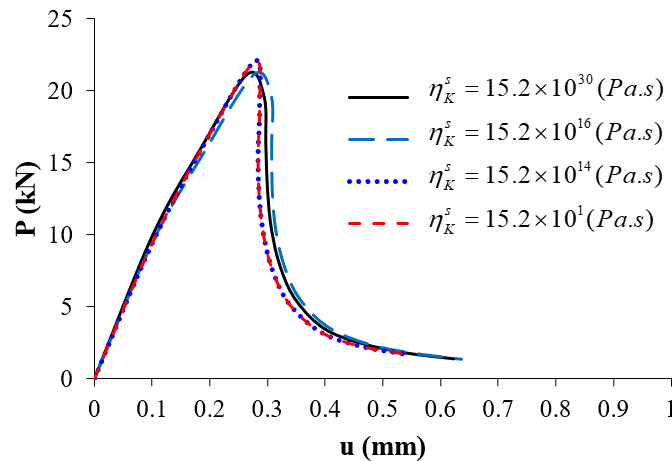


Figure 9. Force-displacement curves when the bulk viscosity of the bulk viscosity of the Kelvin series changes.

Figure 10 presents the results of the investigation into the influence of coefficient η_M^d . The results indicate that this coefficient significantly affects crack propagation within the beam as well as the vertical displacement at the mid-span. In cases where the coefficient surpasses 7.75×10^{16} (Pa.s), crack development occurs, but the value of P_{max} remains constant.

Additionally, the post- P_{\max} curve's ductility is significantly dependent on the coefficient η_M^d . However, when 7.75×10^{15} (Pa.s), crack propagation does not occur.

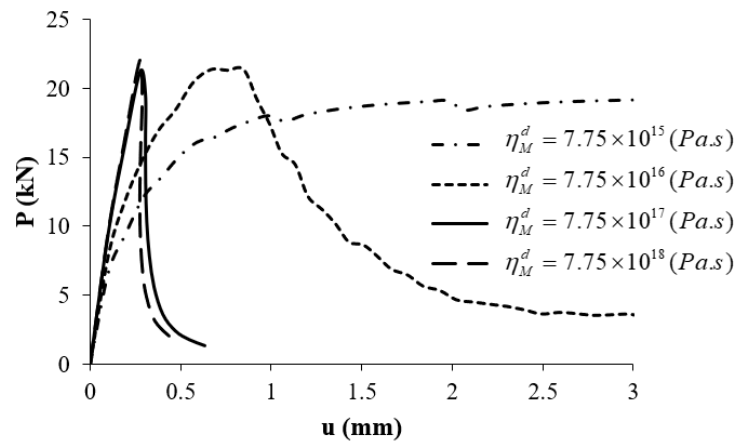


Figure 10. Force-displacement curves when the bulk viscosity of the shear viscosity of the Maxwell series changes.

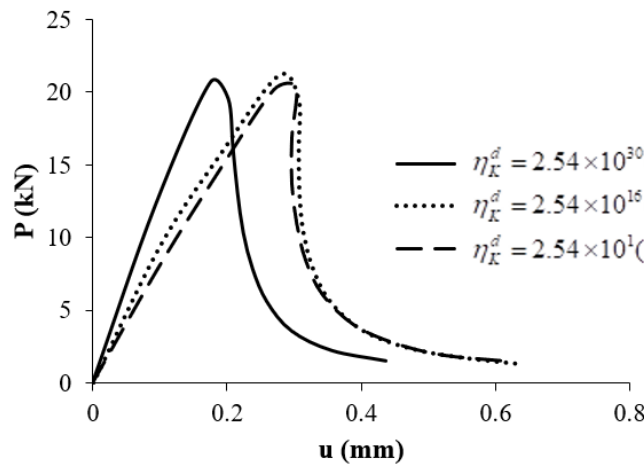


Figure 11. Force-displacement curves when the bulk viscosity of the shear viscosity of the Kelvin series changes.

The results of the investigation into the influence of coefficient η_K^d (Fig. 11) reveal that as the coefficient increases, the displacement corresponding to P_{\max} decreases. The results are in contrast to the investigation of the influence of the coefficient ν_M (Fig. 12), indicating that as ν_M increases, the displacement corresponding to P_{\max} also increases. However, the slope after reaching P_{\max} appears to be unaffected in both cases η_K^d and ν_M .

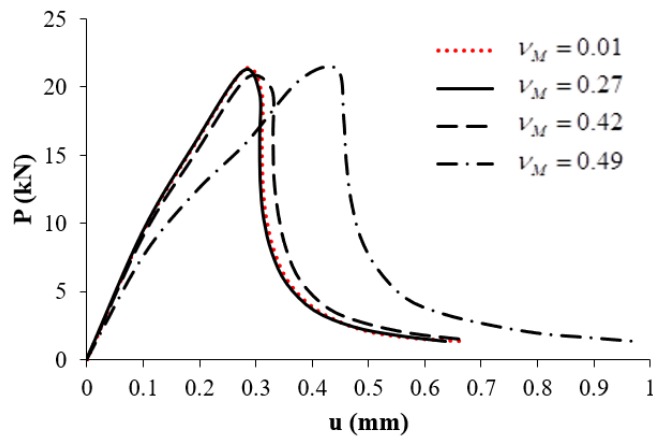


Figure 12. Force-displacement curves when the bulk viscosity of the Maxwell poisson ratio changes.

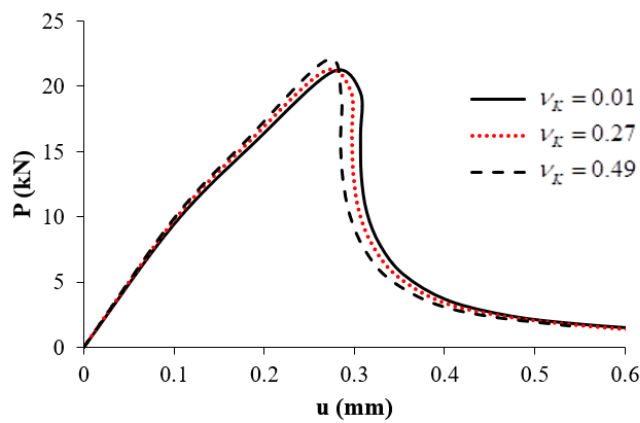


Figure 13. Force-displacement curves when the bulk viscosity of the Kelvin Poisson ratio changes.

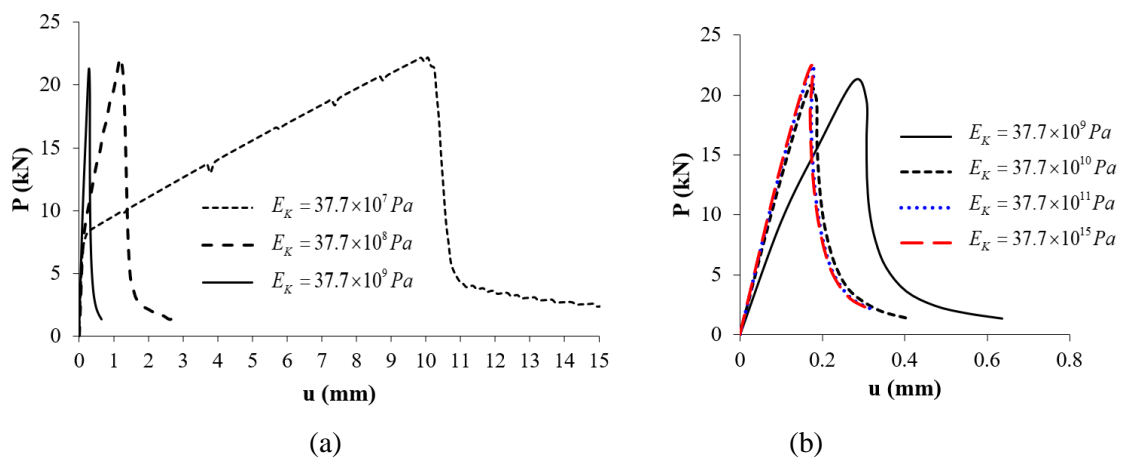


Figure 14. Force-displacement curves when the bulk viscosity of the Kelvin modulus E_K changes: $E_K=37.7 \times 10^7 \div 37.7 \times 10^9$ Pa (a), and $E_K=37.7 \times 10^{10} \div 37.7 \times 10^{15}$ Pa (b).

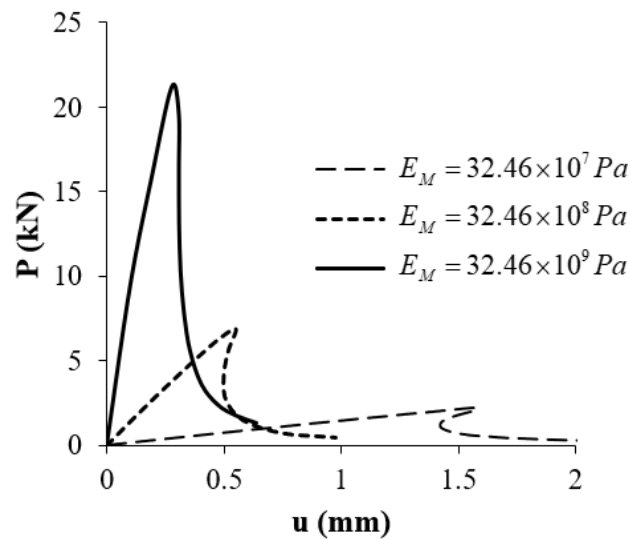


Figure 15. Force-displacement curves when the bulk viscosity of the Maxwell modulus changes.

Similar to coefficient η_K^s , coefficient ν_K exhibits a wide range of variations but has minimal influence on the P-u curve (see Fig. 13). When investigating the value of E_K , the results demonstrate that E_K does not affect the P_{max} value significantly, but it strongly influences the displacement at P_{max} (Fig. 14). The displacement value can decrease proportionally with the increase in E_K (Fig. 14a), but once E_K reaches a high value ($E_K > 37.7 \times 10^{10}$), the displacement decreases to a constant limit (Fig. 14b). Meanwhile, the modulus of elasticity E_M exerts a strong influence on both P_{max} and u . As E_M decreases, P_{max} decreases (approximately three times when E_M is reduced by a factor of 10), and the displacement u increases (approximately three times when E_M is reduced by a factor of 10) as shown in Figure 15.

6. CONCLUSIONS

In conclusion, the current study investigated the fracture properties of concrete through beam simulation with initial crack-depth ratios of 0.2, 0.3, 0.4, 0.5, and 0.6. The findings can be summarized as follows:

Specimens with initial crack-depth ratios of 0.2 and 0.3 exhibited a slightly smaller deflection and more brittle behavior during crack propagation. Besides, it is observed that an increasing the initial crack-depth ratio from 0.2 to 0.6 resulted in a decrease in the maximum load (P_{max}) but a lightly increase in the corresponding displacement.

The simulation model yielded load limit results that approximate experimental outcomes when the elastic modulus (E_M) and Poisson's ratio were known.

The investigation of parameters such as initial crack depth, displacement acceleration, time step, and various coefficients revealed important insights. These parameters influenced the behavior of the P-u curve, including the softening behavior, post-peak response, and crack propagation. The modulus of elasticity E_M emerged as a significant factor, impacting both the maximum load value and displacement. These findings contribute to a deeper understanding

of the structure's response and highlight the importance of considering these parameters in similar simulations.

Furthermore, the accuracy of numerical simulations depends on the availability and accuracy of material properties and viscoelastic models. Further research on obtaining accurate and reliable material properties and model parameters for some kind of material models such as Burger model, Modified Maxwell model can improve the accuracy of numerical simulations. Further research also needs to investigate the effects of specimen size and loading spans on the fracture properties of concrete or textile-reinforced concrete, and the crack opening should be investigated.

REFERENCES

- [1]. Y. Yin, Y. Qiao, S. Hu, Four-point bending tests for the fracture properties of concrete, *Engineering Fracture Mechanics*, 211 (2019) 371-381. <https://doi.org/10.1016/j.engfracmech.2019.03.004>
- [2]. W. Kan, Z. Yang, W. Yin, Simulation of Four-Point Bending Fracture Test of Steel-Fiber-Reinforced Concrete, *Materials*, 15 (2022) 7146. <https://doi.org/10.3390/ma15207146>
- [3]. C. Barris, P. Zubillaga, L. Torres, A review on experimental flexural cracking in FRP reinforced concrete members, In: *Proceedings of the IABSE Symposium, Guimaraes (2019)*. <https://doi.org/10.2749/guimaraes.2019.0088>
- [4]. Y. X. Zhao, H. Xu, W. L. Jin, Concrete cracking process induced by steel corrosion-A review, In: *Proceedings of the Thirteenth East Asia-Pacific Conference on Structural Engineering and Construction (EASEC-13) (2013, September)*, pp. Keynote-Lecture 5.
- [5]. D. Lau, O. Büyüköztürk, Fracture characterization of concrete/epoxy interface affected by moisture, *Mechanics of Materials*, 42 (2010) 1031-1042. <https://doi.org/10.1016/j.mechmat.2010.09.001>
- [6]. W. Dong, X. Zhang, B. Zhang, Q. Wu, Influence of sustained loading on fracture properties of concrete, *Engineering fracture mechanics*, 200 (2018) 134-145. <https://doi.org/10.1016/j.engfracmech.2018.07.034>
- [7]. J. P. Ulfkjaer, Fracture Energy of Normal Strength Concrete, High Strength Concrete and Ultra High Strength Ultra Ductile Fibre Reinforced Concrete, *Proceedings FRAMCOS-2 (1995)* 31-44.
- [8]. M. Leone, G. Centonze, D. Colonna, F. Micelli, M. A. Aiello, Fiber-reinforced concrete with low content of recycled steel fiber: Shear behaviour, *Construction and Building Materials*, 161 (2018) 141-155. <https://doi.org/10.1016/j.conbuildmat.2017.11.101>
- [9]. N. H. Tran, T. T. N. Nguyen, T. H. Vo, Enhancing the efficiency of textile reinforced concrete (TRC) for strengthened reinforced concrete beams, *International conference-Construction science and Technology toward sustainable development, IBST-Hanoi, (2023, November 10th)*, pp. 135-142 (in Vietnamese).
- [10]. S. T. Nguyen, *Propagation de fissures et endommagement par microfissures des matériaux viscoélastiques linéaires non vieillissants (in French)*, Doctoral thesis, Université Paris Est, 2010.